Research Square

Preprints are preliminary reports that have not undergone peer review.
They should not be considered conclusive, used to inform clinical practice,
or referenced by the media as validated information.

Modeling efficiency penalties of narrow-bandgap perovskites in Si-based tandem solar cells: Incorporating luminescent coupling at non-ideal absorption

Rolf Brendel

brendel@solar.uni-hannover.de

Institute for Solid State Physics, Leibniz Universität Hannover https://orcid.org/0000-0001-8259-564X

Article

Keywords:

Posted Date: August 20th, 2026

DOI: https://doi.org/10.21203/rs.3.rs-10667647/v1

License: This work is licensed under a Creative Commons Attribution 4.0 International License.
Read Full License

Additional Declarations: There is **NO** Competing Interest.

Modeling efficiency penalties of narrow-bandgap perovskites in Si-based tandem solar cells: Incorporating luminescent coupling at non-ideal absorption

Rolf Brendel[1,2]

[1]*Institute for Solid State Physics, Leibniz University Hannover, Germany*

[2]*Institute for Solar Energy Research Hamelin (ISFH), Germany*

For silicon-based tandem devices, accurate prediction of the efficiency potential for sub-optimal band gap perovskites depends on quantifying luminescent coupling (LC) that is sensitive to the band gap and the thickness of the top cell. Here, we present a detailed balance model that accounts for these dependencies and derives LC from first principles. This enables a reliable quantification of the efficiency penalty incurred by narrow band gap perovskites (~1.57 eV) as compared to top cells with optimal band gaps (~1.7 eV) in Si-based tandems. We find that the relative efficiency penalty is 5% for two-terminal and 2% for four-terminal configurations—a surprisingly small disadvantage that coincides with a reduction of the optimal absorber thickness by more than half. Narrow band gap perovskites may therefore have a previously underestimated relevance for tandem photovoltaics, particularly if their modest efficiency losses are outweighed by gains in stability and material savings.

1 Introduction

Since the seminal work of Shockley and Queisser,[1,2] detailed balance (DB) modeling has been widely used to determine optimal band gaps in photovoltaics.[3,4] Such analysis led to an efficiency maximizing band gap for the perovskite (Pk) top cell in Si-based tandems or of approximately 1.7 eV at optimal absorber thickness.[5–7] Efficiency is a crucial metric; however, long-term stability is equally important. The future stability limits achievable by the rapidly evolving field of Pk photovoltaics at specific band gaps remain uncertain. As a result, a material's efficiency advantage at a given band gap could potentially be offset by its disadvantage in stability. Conversely, understanding how a lower band gap material's reduction in efficiency potential might be compensated by higher stability compared to larger band gap materials requires a model that can reliably and quantitatively compare the efficiency potentials across different band gaps.

Such a model should ideally be fully compatible with the established DB modeling of single junction crystalline Si cells, which defines a benchmark efficiency potential of 29.4% at a Si wafer thickness of ~100 µm.[8–10] Accordingly, the Pk–Si DB model needs to incorporate the AM1.5G solar spectrum, wavelength-dependent optical constants for both Pk and Si, ideal anti-reflection on both sides of the Pk layer, ideal back reflector, Lambertian light trapping, quasi-Fermi levels that are constant throughout the cells, Auger recombination in Si, and total internal reflection effects for diffuse light incident upon less optically dense materials. Notably, Pks with smaller band gaps in Pk–Si tandems absorb a greater fraction of the solar spectrum, resulting in surplus photogeneration in the top cell that can be transferred to the bottom cell via luminescent coupling (LC). Therefore, accurate modeling of LC in non-black cells is thus particularly important when simulating tandems with small-gap Pks.

Almansouri et al.[11] extended established models by abandoning the Shockley-Queisser assumption of an abrupt absorption onset; however, they did not consider luminescent coupling effects. Futscher et al.[12] were the first to incorporate LC into DB modeling of perovskite–silicon (Pk–Si) tandem efficiencies, though still under the simplification of unity absorption for all photons with energies above the band gap. Rühle[7] further advanced the field by including LC in Pk–Si tandem efficiency calculations, yet maintaining the assumption of an infinitely sharp absorption edge. In their model, reduced absorption in the top cell was represented by a wavelength-independent factor A, which was applied to both, to solar absorption and to the LC into the bottom cell. This approach, however, disregards the different density of photon states in air and in the bottom cell. Even a fully black $A = 1$ cell will emit more power into the bottom cell than into air. Nelder et al.[5] were the first to simultaneously optimize both band gap and thickness of the top cell, but luminescent coupling effects were not included. Jäger et al.[6,13] incorporated LC in their analysis but did not account for the fact that varying the band gap intrinsically affects LC. Nguyen et al.[14] linked experimental LC efficiencies to energy yield simulations based on transfer-matrix calculations using Kramers–Kronig-consistent optical data; however, as their LC values were empirically derived,[15] the dependence of LC on varying band gap could not be captured. Allen et al.[16] introduced Auger recombination in the Si bottom cell and used the reciprocity between electroluminescence and experimental external quantum efficiency (EQE) to treat non-radiative recombination in the Pk top cell. While innovative, this method cannot disentangle the effects of optical device design from electronic material quality, since EQE

reflects both. Moreover, LC was omitted. Fell et al.[17] combined numerical transport modeling of an Auger-limited Si cell with Shockley–Queisser-type of DB modeling of the Pk cell and found that the Si thickness has only a minor impact on the tandem performance. Luminescent coupling was introduced by an additional coupling constant, thereby disregarding the variation of the refractive index with the band gap.

To date, none of the aforementioned approaches derive luminescent coupling rigorously from basic physical principles for non-black cells. Addressing this deficiency, our work integrates and extends previous models to present a physically grounded and comprehensive treatment of LC, specifically accounting for wavelength-dependent absorption in non-ideal (non-black) top cells. The optical and electronic modeling framework is described in the "Methods" section and detailed in the Supplementary Information (SI). The "Results" section demonstrates the first application of this improved model to the question of efficiency penalty for smaller than optimal band gaps.

2 Results

2.1 Two terminal perovskite-Si tandems

Figure 1 shows the simulated results for a two-terminal (2T) configuration under one sun AM1.5G illumination and no light trapping in the top cell. The thickness W_1 of Pk is varied. We assume an intrinsically limited Si wafer of thickness of 150 µm with a Lambertian mirror of unity reflectance on the rear. As for the Si benchmark simulations[8–10] interfaces have either unity transmission (while accounting for total internal reflection) or unity reflection at all wavelengths. We construct Kramers-Kronig conform dielectric functions for the Pks form Bailey's fit[18] to spectroscopic ellipsometry data of the archetypal solar cell material $CH_3NH_3PbI_3$ ($MAPbI_3$) applying the Tauc-Lorenz model.[19,20] See Figures S2 and S3 in the SI. Note that this work labels band gap by intersections in the Tauc plot to become conform with the typical labeling by experimentalists.

Figure 1 (a) illustrates key device characteristics as a function of perovskite (Pk) top cell thickness W_1. Solid lines represent calculations for a $MAPbI_3$-type of gap with $E_{g1} = 1.57$ eV, while dotted lines show results with E_{g1} optimized for maximum tandem efficiency η. (b) The highest tandem efficiency, 41.84%, is achieved at W_1 =1500 nm when E_{g1} is optimized. We consider 1500 nm as a practical upper limit for production. (b) As the top cell becomes thicker, the absorption onset sharpens, causing the optimal band gap to approach the value reported in the literature under the assumption of abrupt absorption onset.[5–7,21] For a set Pk thickness of 412 nm, the efficiency maximizes at E_{g1}= 1.57 eV. For this band gap, the maximum efficiency of 39.86% is, however, reached at $W_1 = 733$ nm. (c) The short-circuit current densities $J_{sc,1}$ (top cell, blue) and $J_{sc,2}$ (bottom cell, red) are equal at a thickness of 385 nm, indicating current matching. For thicknesses W_1 >385 nm and E_{g1}= 1.57 eV, the tandem current becomes limited by the bottom cell. In contrast, when the optimal band gap is chosen, current limitation by the bottom cell persists across all thicknesses. (d) A fraction of the radiative recombination in the top cell gives rise to the

luminescent coupling (LC) current density $J_{1\to2}$. At $W_1 =$ 412 nm this current is $J_{1\to2}$= 0.69 mA/cm^2 at the maximum power point, increasing steeply with thickness for narrow band gaps (solid lines), and reaching a large value of 4.37 mA/cm^2 at $W_1 = 1500$ nm. In comparison, the coupling current density $J_{2\to1}$ emitted from the bottom Si cell and absorbed in the Pk top cell (not shown) remains below 1 nA/cm^2 and is therefore negligible. Panels (e) and (f) display the calculated external quantum efficiency Q_e, as defined in Eq. (S55) of the SI, and the luminescent coupling efficiency η_{LC}. The latter at is the ratio of luminesce absorbed in the bottom cell over luminescence emitted to the outside.[15] Notably, η_{LC} depends on both, the thickness and the band gap. The coupling efficiency η_{LC} is thickness-dependent because a fraction of the upwards emitted luminescent light is internally reflected at the front and subsequent propagation to the bottom cell causes a thickness-dependent attenuation. The blue solid line is an estimation of η_{LC} that builds on this interpretation. See (S54) for more details.

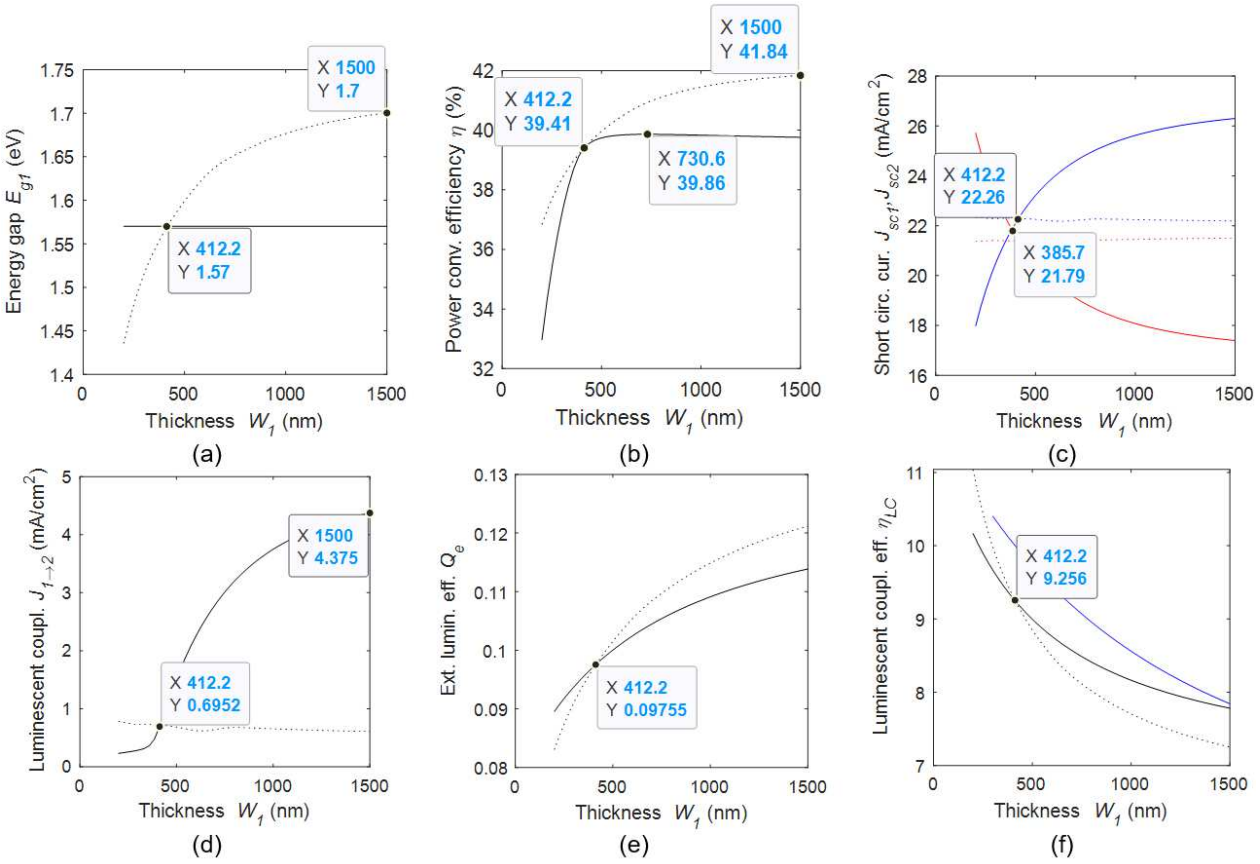

Figure 1: Black solid lines: Energy gap for the reference case with fixed $\mathrm{E_{g1}} = 1.57$ *eV. Black dotted lines: Case with optimized energy gap* $\mathrm{E_{g1}}$. *X and Y values of data discussed in the text are boxed. (a) Bandgap energy* $\mathrm{E_{g1}}$. *(b) Efficiencies at Pk thickness* $\mathrm{W_1}$. *(c) Generation current densities* $\mathrm{J_{sc,1}}$ *of the top cell 1 (in blue) and* $\mathrm{J_{sc,2}}$ *of the bottom cell 2 (in red). (d) Photon coupling current density* $\mathrm{J_{1\to2}}$ *emitted from the top and absorbed in the bottom cell. (e) External luminescent efficiency* $\mathrm{Q_e}$. *(f) Luminescent coupling efficiency* η_{LC}. *The blue line is a theoretical estimate from* (S54) *when evaluated at* $\mathrm{E_{g1} + qV_{th}/2}$.

2.2 Efficiency penalty and thickness savings

Tandem efficiencies and top cell thickness of the reference case discussed in section 2.1 are listed in row (a) of Table 1. The narrow gap penalty in efficiency potential is 4.7% relative. The optimal thickness is 51% lower for the narrow gap than for the optimal gap. The question arises to what extend these figures are sensitive to various of our assumptions. In row (b) we assume an internal luminescent efficiency $Q_i = 0.7$ instead of unity. The results are similar: Here the efficiency penalty is 5.6% and the thickness saving is 72%. (c) Ideal Lambertian light scattering by the front surface of the Pk ($l_f = 1$) instead of no light trapping ($l_f = 0$) also results in about 5% penalty and more than 50% thickness saving. Surprisingly, an ideal scattering in the Pk increases the efficiency by only 0.17 and 0.20% points, for fixed and optimal band gap, respectively. Light trapping is thus much less important in Pks than in Si. (d) Adding a dichroic mirror between the cells that switches from unity reflection to unity transmission at an optimized wavelength $\lambda_c = 722$ nm (see (S50) for the definition) improves the device with the optimal gap by 0.29% points of efficiency. For the narrow gap case the optimization pushes λ_c to a value that lets all luminescence light pass. This shows that the narrow gap material heavily relies on luminescent coupling. (e) When enhancing the non-radiative recombination in the top cell to 30% ($Q_i = 0.7$ instead of 1) and simultaneously enhancing the non-radiative recombination current $J_{0,SRH,Si}$ in the Si cell from zero to $10\ \mathrm{fAcm^{-2}}$, we again find a similar efficiency penalty and thickness savings. (f): The efficiency penalty remains at about 5% in a voltage-matched ($2\,V_2 = V_1$) three-terminal (3T) configuration. Here, however, we do no longer find an advantage in optimal thickness. (g) Comparing narrow gap and optimal gap performance in a 4T configuration reduces the efficiency penalty to only 2.2%. (h) When allowing for a dichroic mirror in a 4T configuration we find the largest efficiency potential among all simulation in this paper amounting to 42.6%, again with a relative efficiency penalty of only 2.1% and no thickness saving.

Table 1: Comparing the simulated efficiency and optimal thickness $\mathrm{W}_1 \in$ [0 nm,1500 nm] *for a gap of* $\mathrm{E}_{\mathrm{g1}} = 1.57\ \mathrm{eV}$ *and for and optimal bandgap* $\mathrm{E}_{\mathrm{g1}} \in$ [1.4 eV,1.9 eV]. Efficiency penalty and thickness gain are relative values.

		Efficiency	Opt. Gap	Efficiency	Efficiency loss	Thickness	Thickness	Thickness saving
		$\eta_{1.57\mathrm{eV}}$ (%)	$\mathrm{E}_{\mathrm{g1\ opt}}$ (eV)	$\eta_{\mathrm{Eg1\ opt}}$ (%)	$\Delta\eta/\eta_{\mathrm{Eg1\ opt}}$ (%)	$\mathrm{W}_{1.57\mathrm{eV}}$ (nm)	$\mathrm{W}_{\mathrm{Eg1\ opt}}$ (nm)	$\Delta W/\mathrm{W}_{\mathrm{Eg1\ op}}$ (%)
(a)	Reference case	39.86	1.70	41.82	4.7	733	1500	51
(b)	$Q_i = 1 \rightarrow 0.7$	38.79	1.71	41.03	5.6	419	1500	72
(c)	$l_f = 0 \rightarrow 1$	40.03	1.72	42.11	4.9	477	1500	68
(d)	$\lambda_c = 0 \rightarrow > 0$	39.87	1.73	42.60	6.4	706	1500	53
(e)	$J_{0,SRH,Si} = 0 \rightarrow 10\ \mathrm{fAcm^{-2}}$ $Q_i = 1 \rightarrow 0.7$	37.87	1.72	40.17	5.7	413	1500	72
(f)	2T → 3T	39.61	1.79	42.00	5.7	1500	1500	0
(g)	2T → 4T	41.08	1.79	42.01	2.2	1500	1500	0
(h)	2T → 4T & $\lambda_c = 0 \rightarrow > 0$	41.74	1.74	42.61	2.1	1500	1500	0

3 Discussion

We present detailed balance (DB) efficiency calculations for perovskite/silicon tandem cells in two-, three-, and four-terminal configurations, with luminescent coupling (LC) determined from physical principles as established in contemporary single junction DB modeling. The model explicitly accounts for the dependence of LC on the optical properties of the tandem device, primarily determined by band gap and top cell thickness. Being fully analytic, the approach is computationally efficient and readily allows for simultaneous multi-parameter optimization, including identification of maximum power points, optimal band gap, top cell thickness, and, where applicable, switching wavelength for a dichroic mirror.

For full consistency with current silicon cell efficiency benchmarks, we assume unity transmission where not limited by internal reflection. Thin-film interference effects in the perovskite are thus suppressed, thereby justifying the use of thick-film theory in our analysis. By contrast, a dichroic mirror introduces standing wave patterns that render our detailed balance model an approximation. As interference effects tend to average out upon spectral integration and because of roughness, and as we showed that overall efficiency is only weakly dependent on the Pks' light-trapping regime we speculate that this approximation is valid.

Consistent with previous findings, the optimal band gap for the perovskite top cell is approximately 1.7 eV for 2T configurations. Accordingly, substantial research efforts are targeting the development and fabrication of perovskite tandem cells with band gaps in this optimal range. Nonetheless, there is emerging experimental evidence indicating that smaller-band-gap perovskite materials may also hold significant relevance provided their efficiency penalty is not too large:

(i) Narrow gap materials did show open circuit voltages that are closer to their respective radiative limit than the voltages of wide gap materials.[22,23] This is at least partly due to less compositional inhomogeneities[24] and photoinduced phase segregation[25,23,26,27] that enhances non-radiative recombination.[26]

(ii) Smaller bandgap materials enable thinner Pk layers while still achieving current matching in 2T devices that is supported by LC. Depositing thinner layers requires less time and could widen the bottleneck of slow deposition rates, in particular for vacuum deposition techniques.[28] Processing the Pk absorber accounts for about 5% of the Pk-Si module cost.[29] Using thinner films does thus also offer a minor potential for cost savings.

(iii) Thinner cells due to smaller gaps will carry less toxicity per area. This is relevant in case future PV modules will still contain Pb.[30,31]

(iv) Low-gap top cells allow for more rear-side benefit in bifacial tandems.[6]

Here, we show that $MAPbI_3$-type perovskites in 2T configuration exhibit an efficiency penalty of only 4.7% when compared to materials with the optimal band gap. The penalty is less than the penalties of 6.2% that can be read from Fig. 3b of previous work[7] using less rigorous modelling of LC. Work fully neglecting LC calculated a relative penalty as large as 25% (Fig. 1b, 2T, one-sun in ref. [32]). Importantly, if future perovskite compositions with ideal band gaps were to degrade just ~5% more than a 1.57 eV material, the latter could ultimately achieve a higher end-of-life efficiency. Scaling from lab to fab remains a costly challenge, with module durability and integration strategies critically depending on the choice of perovskite composition. Our model enables a data-driven selection of band-gap materials by quantifying the efficiency trade-off and allowing performance considerations to be balanced with stability and manufacturing criteria.

An additional advantage of small-band-gap perovskites is their suitability for high-efficiency single-junction modules without requiring major changes to Pk processes used for tandem cells. In a 4T configuration, the relative efficiency loss for a small-band-gap device is only 2.1% compared to the ideal-gap scenario. The top cell alone contributes 30.6% points to the overall device efficiency (see Table S3*,* 4T) and is thus attractive as single junction cell surpassing the 29.4% efficiency benchmark of Si. Here, and similar for a 3T case (see Table S3, 3T), the Pk cell contributes about three times the power output of the silicon cell. This, combined with the superior radiation tolerance of perovskite cells relative to silicon,[33] could become particularly advantageous for applications in space environments.

For 1.57 eV material in any of the investigated 2T configurations we always find thickness savings above 50% when comparing to the optimal-band-gap case (see Table S2, 2T). This halves any future toxicity load, e.g. from Pb, and also decreases deposition time which is particularly relevant for vacuum process.[28]

Taken together, our results shall motivate a reassessment of the strategic value of developing Pk–Si tandem modules with lower-band-gap perovskite absorbers, which may offer practical advantages in photovoltaic yield stability at marginally reduced theoretical efficiency.

4 Methods

Figure 2 (a) though (d) illustrates the physics of our DB model. See SI for details. The tandem device consists of a top cell of thickness W_1 with absorption index α_1 and refractive index n_1. The bottom cell shall be crystalline Si. The front surface f, the interface i between the two subcells, and the back reflector b have a lossless transmission T_f, T_i, and reflectance R_b, respectively. We consider propagation of specular light (black arrows) and diffusive light (red arrows). The interfaces f and b can convert fractions l_f and l_b from specular to fully diffusive light as is indicated by a dashed blue arrow for the back reflector. We assume a Lambertian back reflector ($l_b = 1$). The model describes the propagation of both specular and diffuse light by photon fluxes taken directly above and below the interfaces, traveling in upward and downward directions. These intensities are depicted by the filled blue dots. The yellow dot indicates the incident AM1.5G solar photon flux, while red circles denote additional photon fluxes arising from radiative recombination propagating up and downwards. Further details can be found in Figure S1 and its accompanying description.

Figure 2 (b) shows specular and fully diffuse light fluxes passing the top cell once. The attenuation factor T_{s1} of specular light (black) is smaller than the factor T_{d1} for diffuse light (red) due to the oblique propagation.[9,34]

Figure 2 (c) is the tandem cell at thermal equilibrium. Anywhere in the top cell is a photon flux $n_1^2\,\phi_{bb}$ (photons per area, time and solid angle) with ϕ_{bb} denoting the vacuum black body radiation. The thermal photon flux from a half sphere into and out of the Pk interfaces is $\pi\, n_1^2 \phi_{bb}$ (photons per area and time). The portion of the flux into the PK being absorbed in the Pk is $(1 - T_{d1})$. These absorption processes are in detailed balance to all radiative recombination processes. Thus, the equilibrium luminescence flux at the interfaces from within the cell and without any interface interaction is $G_1 = \pi\, n_1^2 \phi_{bb}\ (1 - T_{d1})$.

Knowing all reflection, transmission and attenuation factors we solve an equation system for the interface intensities shown as dots in Figure 2 (a). See equations (S3) through (S20) in the SI. With the sun (yellow dot) on and the luminescence off (red dots) we calculate the absorption A_1 of sunlight in the top cell. With the sun off and the luminescence on we add the intensities G_1 to the respective interface intensities and then solve for the probability $A_{1\to2}$ that luminescence from cell 1 is absorbed in cell 2. We also determine the probability $A_{1\to0}$ for escaping to the front medium and the parasitic absorption $A_{0\to b}$ of luminescence in the back reflector. Adding the luminescence intensity and solving is the core of the approach that we therefore term ALIAS.

Figure 2 (d) illustrates all processes to be considered for the total recombination current $J_{0,1}$of the top cell.[35] It has a contribution $q\ W_1\ \int_{\lambda=0}^{\infty} \alpha_1 4\pi n_1^2 \Phi_{bb} d\lambda \left(\frac{1}{Q_{i,1}} - 1\right)$ for the non-radiative recombination that vanishes at unity internal luminescence efficiency $Q_{i,1}$ with q denoting the elementary charge. Photons from radiative recombination contribute to the recombination current if they either escape into the front medium with probability $A_{0\to1}$, are absorbed in the bottom cell with probability $A_{1\to2}$, or are parasitically absorbed elsewhere, e.g. in the back reflector, with probability $A_{0\to b}$. The respective three contributions to the recombination currents are $q\ \int_{\lambda=0}^{\infty} 2\ G_1 A_{1\to x}\ d\lambda$ with $x = 0,2,b$. Luminescent coupling transfers photogeneration from the top to the bottom cell. When accounting for this, the current-voltage (I-V) curve of the Pk cell is calculated in the usual way with the above discussed contributions to the recombination current. The short circuit current of the top cell is derived from solar absorption A_1. See (S47) for the I-V curve of the Pk cell and (S48) for that of the Si cell.

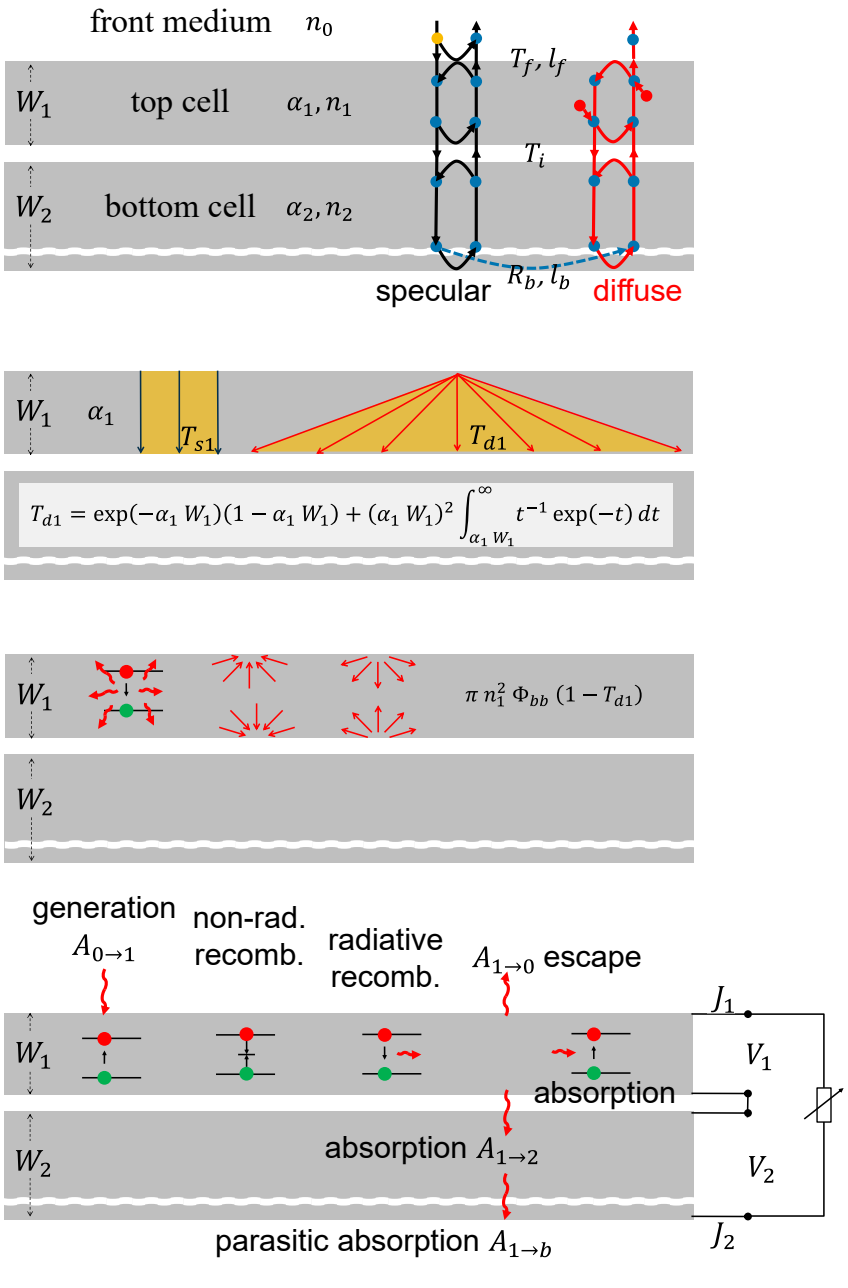

Figure 2: Illustration of the model for calculating efficiencies of tandem cells with a detailed balance model. (a) Material and interface parameters and light fluxes. (b) Single passes of specular and diffusive light attenuate differently by factors T_{s1} *and* T_{d1}*, respectively. (c) Before interacting with any interfaces, radiative recombination causes a luminescence flux* $\pi\, n_1^2 \Phi_{bb}\, (1 - T_{d1})$ *at either interface (red circles in (a)). (d) Collecting various process probabilities* A *allows calculating the short-circuit and the recombination current of the top cell (see (S47) and (S48)).*

5 Acknowledgements

I am grateful to Hans-Joachim Queisser (Max-Planck Institute for Solid State Research, Stuttgart) who passed away last year. I am still profiting from both, his work and support. Thanks also to T. Wietler (Leibniz Universität Hannover) for checking optical models, and to R. Peibst (ISFH) and N.-P. Harder (Total Energies) for discussions inspiring this work.

6 References

1. Shockley, W. & Queisser, H. J. Detailed balance limit of efficiency of p-n junction solar cells. *J Appl Phys* **32,** 510; 10.1063/1.1736034 (1961).

2. Shockley, W. & Queisser, H. J. Detailed Balance Limit of Efficiency of p-n Junction Solar Cells. *J Appl Phys* **32,** 510–519; 10.1063/1.1736034 (1961).

3. Henry, C. H. Limiting efficiencies of ideal single and multiple energy gap terrestrial solar cells. *J Appl Phys* **51,** 4494–4500; 10.1063/1.328272 (1980).

4. Vos, A. de. Detailed balance limit of the efficiency of tandem solar cells. *Journal of Physics D: Applied Physics* **13,** 839; 10.1088/0022-3727/13/5/018 (1980).

5. Neder, V., Tabernig, S. W. & Polman, A. Detailed-balance efficiency limits of two-terminal perovskite/silicon tandem solar cells with planar and Lambertian spectral splitters. *J. Photon. Energy* **12**; 10.1117/1.JPE.12.015502 (2022).

6. Jäger, K., Tillmann, P., Katz, E. A. & Becker, C. Perovskite/Silicon Tandem Solar Cells: Effect of Luminescent Coupling and Bifaciality. *Solar RRL* **5**; 10.1002/solr.202000628 (2021).

7. Rühle, S. The detailed balance limit of perovskite/silicon and perovskite/CdTe tandem solar cells. *physica status solidi (a)* **214**; 10.1002/pssa.201600955 (2017).

8. Richter, A., Hermle, M. & Glunz, S. W. Reassessment of the Limiting Efficiency for Crystalline Silicon Solar Cells. *IEEE J. Photovoltaics* **3,** 1184–1191; 10.1109/jphotov.2013.2270351 (2013).

9. Schäfer, S. & Brendel, R. Accurate calculation of the absorptance enhances efficiency limit of crystalline silicon solar cells with Lambertian light trapping. *IEEE J. Photovoltaics* **8,** 1156–1158; 10.1109/jphotov.2018.2824024 (2018).

10. Niewelt, T. *et al.* Reassessment of the intrinsic bulk recombination in crystalline silicon. *Solar Energy Materials and Solar Cells* **235,** 111467; 10.1016/j.solmat.2021.111467 (2022).

11. Almansouri, I., Ho-Baillie, A., Bremner, S. P. & Green, M. A. Supercharging Silicon Solar Cell Performance by Means of Multijunction Concept. *IEEE J. Photovoltaics* **5,** 968–976; 10.1109/JPHOTOV.2015.2395140 (2015).

12. Futscher, M. H. & Ehrler, B. Efficiency Limit of Perovskite/Si Tandem Solar Cells. *ACS Energy Letters* **1,** 863–868; 10.1021/acsenergylett.6b00405 (2016).

13. Tillmann, P., Jäger, K., Katz, E. A. & Becker, C. Relaxed current-matching constraints by bifacial operation and luminescent coupling in perovskite/silicon tandem solar cells. In *2021 IEEE 48th Photovoltaic Specialists Conference (PVSC),* pp. 1086–1088.

14. Nguyen, K. *et al.* Optimizing energy yield of monolithic perovskite/silicon tandem solar cells in real-world Conditions: The impact of luminescent coupling. *Solar Energy Materials & Solar Cells* **290,** 113730; 10.1016/j.solmat.2025.113730 (2025).

15. Nguyen, K. *et al.* The Role of Luminescent Coupling in Monolithic Perovskite/Silicon Tandem Solar Cells. *Small* **20,** 2403461; 10.1002/smll.202403461 (2024).

16. Allen, T. G., Ugur, E., Aydin, E., Subbiah, A. S. & Wolf, S. de. A Practical Efficiency Target for Perovskite/Silicon Tandem Solar Cells. *ACS Energy Lett.* **10,** 238–245; 10.1021/acsenergylett.4c02152 (2025).

17. Fell, A. *et al.* Elucidating the efficiency limit of silicon-based monolithic tandem cells through the combination of Auger and Shockley–Queisser limits. *EES Sol.* **1,** 1030–1039; 10.1039/D5EL00085H (2025).

18. Bailey, C. G., Piana, G. M. & Lagoudakis, P. G. High-energy optical transitions and optical constants of $CH_3NH_3PbI_3$ measured by spectroscopic ellipsometry and spectrophotometry. *The Journal of Physical Chemistry C* **123,** 28795–28801; 10.1021/acs.jpcc.9b08903 (2019).

19. Jellison, G. E. & Modine, F. A. Parameterization of the optical functions of amorphous materials in the interband region. *Applied Physics Letters, USA* **69,** 371–373; 10.1063/1.118064 (1996).

20. Jellison, G. E. & Modine, F. A. Erratum: ‘‘Parameterization of the optical functions of amorphous materials in the interband region’’ [Appl. Phys. Lett. 69 , 371 (1996)]. *Applied Physics Letters, USA* **69,** 2137; 10.1063/1.118155 (1996).

21. Lim, J., Park, N.-G., Il Seok, S. & Saliba, M. All-perovskite tandem solar cells: from fundamentals to technological progress. *Energy Environ. Sci.* **17,** 4390–4425; 10.1039/d3ee03638c (2024).

22. Leijtens, T., Bush, K. A., Prasanna, R. & McGehee, M. D. Opportunities and challenges for tandem solar cells using metal halide perovskite semiconductors. *Nat. Energy* **3,** 828–838; 10.1038/s41560-018-0190-4 (2018).

23. Yang, T. C.-J., Fiala, P., Jeangros, Q. & Ballif, C. High-Bandgap Perovskite Materials for Multijunction Solar Cells. *Joule* **2,** 1421–1436; 10.1016/j.joule.2018.05.008 (2018).

24. Ongaro, C., Othman, M., Ballif, C., Wolff, C. M. & Hessler-Wyser, A. Unraveling bulk degradation mechanisms of wide-bandgap perovskite absorbers for tandem applications. *EES Sol.* **2,** 293–314; 10.1039/d5el00199d (2026).

25. Huang, N. & Qiu, L. Toward stable wide-bandgap perovskite solar cells: Comprehensive review of degradation mechanisms and mitigation strategies. *Materials Today Energy* **53,** 102010; 10.1016/j.mtener.2025.102010 (2025).

26. Cui, Z., Zhang, Q., Bai, Y. & Chen, Q. Issues of phase segregation in wide-bandgap perovskites. *Mater. Chem. Front.* **7,** 1896–1911; 10.1039/D2QM01341J (2023).

27. Gil-Escrig, L. *et al.* Efficient and Thermally Stable Wide Bandgap Perovskite Solar Cells by Dual-Source Vacuum Deposition. *Advanced Functional Materials* **33**; 10.1002/adfm.202214357 (2023).

28. Abzieher, T. *et al.* Vapor phase deposition of perovskite photovoltaics: short track to commercialization? *Energy Environ. Sci.* **17,** 1645–1663; 10.1039/D3EE03273F (2024).

29. Cordell, J. J., Woodhouse, M. & Warren, E. L. Technoeconomic analysis of perovskite/silicon tandem solar modules. *Joule* **9**; 10.1016/j.joule.2024.10.013 (2025).

30. Liu, D. *et al.* Inhibition of Lead Toxicity of Perovskite Solar Cells. *Advanced Energy Materials* **16**; 10.1002/aenm.202505840 (2026).

31. Lin, D. *et al.* Mitigating lead toxicity towards safer commercialization of perovskite solar cells. *Nat. Energy* **11,** 805–817; 10.1038/s41560-026-02037-2 (2026).

32. Yu, Z., Leilaeioun, M. & Holman, Z. Selecting tandem partners for silicon solar cells. *Nat. Energy* **1,** 16137; 10.1038/NENERGY.2016.137 (2016).

33. Lang, F. *et al.* Proton Radiation Hardness of Perovskite Tandem Photovoltaics. *Joule* **4,** 1054–1069; 10.1016/j.joule.2020.03.006 (2020).

34. Brendel, R. Physical limitations to crystalline thin-film silicon solar cells, p. 21. Habilitation Thesis. University of Erlangen-Nuremberg, Erlangen, Germany, https://d-nb.info/965246515 (2002).

35. Rau, U., Paetzold, U. W. & Kirchartz, T. Thermodynamics of light management in photovoltaic devices. *Phys Rev B* **90,** 35211; 10.1103/PhysRevB.90.035211 (2014).

36. Brendel, R. *et al.* Breakdown of the efficiency gap to 29% based on experimental input data and modeling. *Prog Photovoltaics Res Appl* **24,** 1475–1486; 10.1002/pip.2696 (2016).

37. Brendel, R. *Thin-Film Crystalline Silicon Solar Cells*; ISBN 3-527-40376-0 (Wiley, 2003).

38. Abramowitz, M. & Stegun, I. A. (eds.). *Handbook of Mathematical Functions. With formulas, graphs, and mathematical tables.* 9th ed.; ISBN 0-486-61272-4 (Dover Publications, New York, 1972).

39. Manzoor, S. *et al.* Optical modeling of wide-bandgap perovskite and perovskite/silicon tandem solar cells using complex refractive indices for arbitrary-bandgap perovskite absorbers. *Opt. Express* **26,** 27441–27460; 10.1364/OE.26.027441 (2018).

40. Klein, J. *et al.* Limitations of the Tauc Plot Method. *Advanced Functional Materials* **33**; 10.1002/adfm.202304523 (2023).

41. Forouhi, A. R. & Bloomer, I. Optical dispersion relations for amorphous semiconductors and amorphous dielectrics. *Phys. Rev. B* **34,** 7018–7026; 10.1103/PhysRevB.34.7018 (1986).

42. Löper, P. *et al.* Complex Refractive Index Spectra of CH3NH3PbI3 Perovskite Thin Films Determined by Spectroscopic Ellipsometry and Spectrophotometry. *The journal of physical chemistry letters* **6,** 66–71; 10.1021/jz502471h (2015).

Supplementary Information

Modeling efficiency penalties of small-bandgap perovskites in Si-based tandem so-lar cells: Incorporating non-ideal absorption and luminescent coupling

Rolf Brendel[1,2]

[1] Institute for Solar Energy Research Hamelin (ISFH)

[2] Institute for Solid State Physics, Leibniz University Hannover (LUH)

The Supplementary Information applies the section titles and section numbering of the main text but preceded by an “S”.

Section “S2 Results” provides more detailed information on the simulations results from applying the model.

Section “S4 Methods” explains and derives the model in much more detail than the main text of the paper.

S2 Results

S2.2 Efficiency penalty and thickness savings

Sensitivity to non-radiative recombination and ideal Lambertian light trapping:

Table S1: Simulated efficiencies of the small bandgap case E_{g1} = 1.57 eV and the optimal bandgap case in a 2T configuration and at optimal thickness $W_1 \in$ [0 nm,1500 nm]. We consider ideal and non-ideal internal luminescence efficiency Q_i and cases without and with Lambertian light trapping l_f in the top cell. The bottom silicon cell is $W_1 = 150\ \mu m^+$ thick and is limited by intrinsic Auger recombination. The transparency from top to bottom cell is ideal ($\lambda_c = -1\ nm^+$). Values that were set are indexed with a "+" while parameters that were optimized for maximum efficiency are marked with a "". Boxed table entries are discussed in the text.*

	$l_f = 0^+$						$l_f = 1^+$,					
	$Q_i = 1^+$			$Q_i = 0.7^+$			$Q_i = 1^+$			$Q_i = 0.7^+$		
E_{g1} fix or optimized	fix	opt.	Δ (%)	fix	opt.	Δ (%)	fix	opt.	Δ (%)	fix	opt.	Δ (%)
E_{g1} (eV)	1.57⁺	1.70*		1.57⁺	1.71*		1.57⁺	1.72*		1.57⁺	1.72*	
W_1 (nm)	733*	1500*	−51	419*	1500*	−72	477*	1500*	−68	279*	1500*	−81
η (%)	39.86	41.82	−4.7	38.79	41.03	−5.6	40.03	42.11	−4.9	39.07	41.30	−5.4
η_1 (%)	25.44	27.26		24.43	26.52		25.57	27.49		24.68	26.76	
η_2 (%)	14.42	14.56		14.37	14.50		14.46	14.62		14.40	14.54	
J_{sc1} (mA/cm²)	24.75	22.12		22.35	21.84		24.62	22.20		22.45	21.85	
J_{sc2} (mA/cm²)	18.94	21.58		21.35	31.86		19.14	21.57		21.41	21.39	
$J_{1\to2}$ (mA/cm²)	2.943	0.494		0.452	0.135		2.799	0.585		0.525	0.134	
Q_e	0.105	0.121		0.0500	0.0400		0.0994	0.1218		0.0519	0.0403	
η_{LC}	8.51	7.24		9.23	7.21		9.06	7.21		9.76	7.17	

Sensitivity to the terminal configuration:

Table S2: Comparison of the performance of the fixed small band (E_{g1} = 1.57 eV) with the optimal bandgap case with $E_{g1} \in$ [1.4 eV nm,1.9 eV] in 2T, 3T and 4T configuration. Thickness $W_1 \in$ [0 nm,1500 nm] is optimized. We assume ideal internal luminescence efficiency ($Q_i = 1$), no light trapping ($l_f = 0$) in the top cell, and ideal transmission of light from top to bottom cell ($\lambda_c = -1$ nm). The bottom cell is $W_1 = 150$ μm thick and limited by intrinsic Auger recombination. Figures set are indexed with a "+" while parameters optimized are marked with a "". Boxed table entries are discussed in the text.*

	2T			3T			4T		
	E_{g1} fixed	E_{g1} optimal	Δ (%)	E_{g1} fixed	E_{g1} optimal	Δ (%)	E_{g1} fixed	E_{g1} optimal	Δ (%)
E_{g1} (eV)	1.57⁺	1.69*		1.57⁺	1.79*		1.57⁺	1.79*	
W_1 (nm)	733*	1500*	−51	1500*	1500*	±0.0	1500*	1500*	±0.0
η (%)	39.86	41.82	−4.7	39.61	42.00	−5.7	41.08	42.01	−2.2
η_1 (%)	25.44	27.28		28.85	25.65		28.97	25.70	
η_2 (%)	14.42	14.54		10.76	16.35		12.10	16.31	
J_{sc1} (mA/cm²)	24.75	22.38		26.30	19.54		26.30	19.61	
J_{sc2} (mA/cm²)	18.94	21.32		17.40	24.16		17.40	24.09	
$J_{1\to2}$ (mA/cm²)	2.94	0.73		1.21	0.56		1.04	0.56	
Q_e	0.105	0.121		0.114	0.126		0.114	0.126	
η_{LC}	8.51	7.28		7.78	6.92		7.78	6.93	

Sensitivity to applying a dichroic mirror in between the cells:

Table S3: Comparison of the performance of the small bandgap case ($\mathrm{E_{g1}}$ = 1.57 eV) with the optimal case having $\mathrm{E_{g1}} \in$ [1.4 eV nm,1.9 eV] and $\mathrm{W_1} \in$ [0 nm,1500 nm] in 2T, 3T and 4T configuration. The threshold wavelength λ_c of the dichroic mirror is also optimized. We assume an ideal internal luminescent efficiency ($\mathrm{Q_i} = 1$) and no light trapping ($\mathrm{l_f} = 0$) in the top cell. The bottom silicon cell is $\mathrm{W_1} = 150\ \mu\mathrm{m}^+$ thick and limited by Auger recombination. Set values are indexed with a "+" and parameters that result from an optimization are marked with a "". Boxed table entries are discussed in the text.*

	2T			3T			4T		
	E_{g1} fixed	E_{g1} optimal	Δ (%)	E_{g1} fixed	E_{g1} optimal	Δ (%)	E_{g1} fixed	E_{g1} optimal	Δ (%)
λ_c (nm)	649*	722*		799*	709*		798*	721*	
E_{g1} (eV)	1.57⁺	1.73*		1.57⁺	1.76*		1.57⁺	1.74*	
W_1 (nm)	706*	1500*	−53	1500*	1500*	+0	1500*	1500*	±0.0
η (%)	39.87	42.60	−6.4	40.66	42.62	−4.6	41.74	42.61	−2.1
η_1 (%)	25.45	28.19		30.71	27.58		30.65	28.10	
η_2 (%)	14.42	14.41		9.95	15.05		11.10	14.52	
J_{sc1} (mA/cm²)	24.81	21.69		26.78	20.83		26.77	21.62	
J_{sc2} (mA/cm²)	18.87	21.74		16.56	22.61		16.65	21.84	
$J_{1\to2}$ (mA/cm²)	3.01	0.126		0.233	0.179		0.290	0.168	
Q_e	0.105	0.718		0.729	0.624		0.605	0.632	
η_{LC}	8.58	0.393		0.372	0.601		0.654	0.581	

Sensitivity to non-radiative recombination in both cells:

Table S4: Comparison of the performance of the fixed small band (E_{g1} = 1.57 eV) case with the optimal bandgap case and $E_{g1} \in$ [1.4 eV nm,1.9 eV] for the 2T configuration and three values of the recombination current density $J_{0SRH,2}$ of the bottom cell. Thickness $W_1 \in$ [0 nm,1500 nm] is optimized. We assume a non-ideal internal luminescence efficiency $Q_i = 0.7$, no light trapping ($l_f = 0$) in the top cell, and ideal transmission of light from top to bottom cell ($\lambda_c = -1$ nm). The bottom cell is $W_1 = 150$ µm-thick. Figures set are indexed with a "+" while parameters optimized are marked with a "". Boxed figures are discussed in the text.*

	$J_{0SRH,2} = 1$ fA cm^{-2}			$J_{0SRH,2} = 10$ fA cm^{-2}			$J_{0SRH,2} = 100$ fA cm^{-2}		
	E_{g1} fixed	E_{g1} optimal	Δ (%)	E_{g1} fixed	E_{g1} optimal	Δ (%)	E_{g1} fixed	E_{g1} optimal	Δ (%)
E_{g1} (eV)	1.57⁺	1.71*		1.57⁺	1.72*		1.57⁺	1.74*	
W_1 (nm)	417*	1500*	−72	413*	1500*	−72	413*	1500*	−72
η (%)	38.62	40.64	−5.0	37.87	40.17	−5.7	36.67	38.70	−5.2
η_1 (%)	24.39	26.43		24.33	26.45		24.31	26.04	
η_2 (%)	14.23	14.21		13.54	13.72		12.36	12.66	
J_{sc1} (mA/cm^2)	22.32	21.84		22.27	21.69		22.26	21.01	
J_{sc2} (mA/cm^2)	21.38	21.85		21.43	22.01		21.43	22.69	
$J_{1\to2}$ (mA/cm^2)	0.45	0.068		0.46	0.14		0.47	0.074	
Q_e	0.0500	0.0400		0.0501	0.0402		0.0501	0.0408	
η_{LC}	9.24	7.21		9.25	7.19		9.25	7.10	

S4 Methods

We consider a stack of two planar solar cells as sketched in Figure S1 and distinguish specular light (black) and fully randomized light (red) propagation, each with upwards and downwards fluxes. The model has 21 encircled light intensities such and the light intensity from outside I_0,and the specular and diffuses reflections R_s and R_d, respectively. All intensities are meant to be taken directly at the interfaces. The up to four indices of the intensities have the following meanings: The first index is s or d stand for specular or diffusive light. The second index is 1 or 2 and stands for the top or bottom cell the light is propagating in. The third index is t or b and denotes the intensity either at the most top or at the most bottom position *inside* the respective cell. The fourth index is u or d and stands for light propagating either upwards or downwards. The internal luminescence light source in cell 1 is represented by G_1 and that of cell 2 by G_2. The three interfaces may have wavelength dependent optical properties. For the models' application in this paper, we assume, however, that the front surface f, the interface between the cells i have zero reflection and no absorption losses at all wavelengths for specular light. For diffusive this also holds for light passing from a first material into an optically denser second material.

In the opposite direction light transmission is reduced by the ration of the refractive indices square. While the interface i is planar and non-scattering. The front interface f back reflector b may cause partial Lambertian light scatting. The back reflector has the reflectance R_b. The dotted blue arrow indicates the conversion of downward propagating specular light to upward propagating diffuse light. Specular light propagating from one interface to another is reduced in intensity by a factor T_s according to its optical absorption coefficient and by a smaller factor T_d for fully diffuse light.

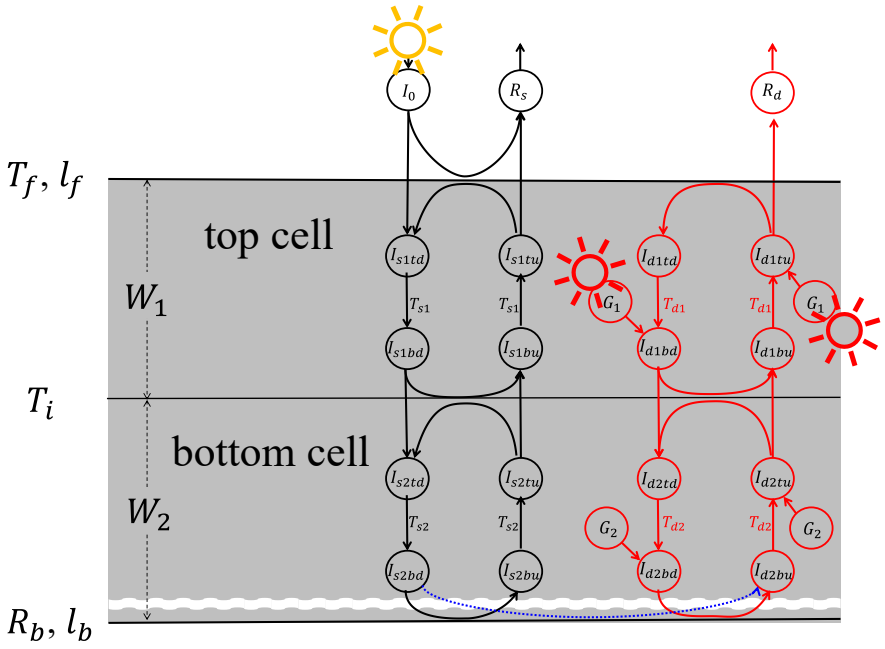

Figure S1: Sketch of the geometry of the optical model and the variables that are calculated. Black and red lines indicate the propagation of specular and fully diffusive light, respectively. Blue lines represent the scattering of specular light into diffusive light. Light of intensity $\mathrm{I}_0 = 1$ *is incident from the non-absorbing surrounding half space onto the front surface* f. *The model is solved for the remaining nine encircled specular and nine encircled diffusive intensities.*

Geometry, interfaces and propagation of light

The surrounding non-absorbing medium shall have the refractive index n_0.The top cell consists of a material with absorption coefficient α_1 and refractive index n_1 and has a thickness W_1. Similarly, the bottom cell consists of a material with absorption coefficient α_2 and refractive index n_2. The bottom cell has a thickness W_2.

The stack has a front surface f with a specular transmission T_f and a Lambertian character l_f.[36] Light that is incident onto an interface with Lambertian character l is by definition considered to be reflected and transmitted both fully randomized with the probability l and to be specularly reflected and transmitted with the probability $(1 - l)$. The depth z is zero at the front surface of the two cells and increases downwards. The intermediate interface i between the top and the bottom cell has a specular transmission T_i and a Lambertian

character l_i, while the third interface b on the back side of the cell has a Lambertian character $l_b$that reflects specular and diffusive light with a reflectance R_b. All these parameters may depend on the wavelength of the light.

Black and red lines in Figure S1 indicate the propagation of specular and of fully diffusive light, respectively. Blue lines represent the transformation of specular light into diffusive light by scattering. Light of intensity 1 is incident from the surrounding non-absorbing medium onto the front interface f. The model uses the nine encircled specular and the nine encircled diffusive intensities.

Specular light propagating through a cell to depth z reduces the intensity by a factor $T_{si}(z)$ according to Lambert Beer's law with $i \in \{1,2\}$ while a smaller factor $T_{di}(z)$ applies to randomized light due to the path length enhancement by oblique incidence. See (S1) and (S2) in the supplementary material for the analytic equations.

All intensity variables have four indices such as I_{d1td}. We distinguish the propagation of specular and fully diffusive light (first subindex s or d), propagation in the top cell or the bottom cell (second index 1 or 2), intensities at the top or bottom interface of the cell (third index t or b), propagating downwards or upwards (fourth index d or u). Specular light paths are shown in black in

and diffusive light paths are shown in red. The blue paths convert Lambertian fractions of specular light into diffusive light.

Figure S1 shows 18 intensities in addition to the three set source intensities I_0,. G_1, and G_2. These 18 variables obey a set of 18 equations that follows from collecting all factors describing absorption, reflection, and scattering along the path of the respective fluxes. With the abbreviations $T_{di} = T_{di}(\alpha_i W_i)$ and $T_{si} = T_{si}(\alpha_i W_i)$ for $i \in \{1,2\}$ we find the set of equations (S3) through (S20) given in the supplementary material.

Specular light propagating through a cell to depth z reduces the intensity by a factor

$$T_{si}(z) \coloneqq \exp(-\alpha_i \mathrm{z}) \tag{S1}$$

according to Lambert Beer's law with $i \in \{1,2\}$. Fully randomized light reduces its' intensity by the factor[37]

$$\begin{aligned} T_{di}(z) &= \frac{\int_0^{\pi/2} \exp\left(-\alpha_i \, \mathrm{z}/\cos(\vartheta)\right) \cos(\vartheta) \, \sin(\vartheta) d\vartheta}{\int_0^{\pi/2} \cos(\vartheta) \, \sin(\vartheta) d\vartheta} \\ &= \exp(-\alpha_i \, z) \, [1 - \alpha_i \, \mathrm{z}] \; + \; [\alpha_i \, \mathrm{z}]^2 \, E_1(\alpha_i \, \mathrm{z}) \end{aligned} \tag{S2}$$

due to the path length enhancement by oblique incidence. Here, $E_1(x) = \int_x^\infty t^{-1} \exp(-t) \, dt$ is the exponential integral function defined for $t > 0$.[38] The full set of equations for the encircled intensities can be read from Figure S1 by following the black, blue and red paths:

$$I_{d1td} = I_{d1tu} * \left[1 - T_f \left[\frac{n_0}{n_1}\right]^2\right] + l_f * \left[I_0\, T_f + I_{s1tu}\left[1 - T_f\right]\right] \quad \text{(S3)}$$

$$I_{d1bd} = I_{d1td} T_{d1} + G_1 \quad \text{(S4)}$$

$$I_{d2td} = I_{d1bd} T_i + I_{d2tu}\left[1 - T_i * \left[\frac{n_1}{n_2}\right]^2\right] + l_i\left[I_{s1bd} T_i + I_{s2tu}[1 - T_i]\right] \quad \text{(S5)}$$

$$I_{d2bd} = I_{d2td} T_{d2} + G_1 \quad \text{(S6)}$$

$$I_{d2bu} = I_{d2bd} R_b + l_b I_{s2bd} R_b \quad \text{(S7)}$$

$$I_{d2tu} = I_{d2bu} T_{d2} + G_2 \quad \text{(S8)}$$

$$I_{d1bu} = I_{d2tu} T_i \left[\frac{n_1}{n_2}\right]^2 + I_{d1bd}[1 - T_i] + l_i\left[I_{s2tu} T_i + I_{s1bd}[1 - T_i]\right] \quad \text{(S9)}$$

$$I_{d1tu} = I_{d1bu}\, T_{d1} + G_1 \quad \text{(S10)}$$

$$R_d = I_{d1tu} T_f \left[\frac{n_0}{n_1}\right]^2 + l_f\left[I_0\left[1 - T_f\right] + I_{s1tu} T_f\right] \quad \text{(S11)}$$

$$I_{s1td} = \left[1 - l_f\right]\, \left[I_0\, T_f + I_{s1tu}\left[1 - T_f\right]\right] \quad \text{(S12)}$$

$$I_{s1bd} = I_{s1td}\, T_{s1} \quad \text{(S13)}$$

$$I_{s2td} = [1 - l_i]\, \left[I_{s1bd} T_i + I_{s2tu}[1 - T_i]\right] \quad \text{(S14)}$$

$$I_{s2bd} = I_{s2td}\, T_{s2} \quad \text{(S15)}$$

$$I_{s2bu} = [1 - l_b]\, I_{s2bd}\, R_b \quad \text{(S16)}$$

$$I_{s2tu} = I_{s2bu}\, T_{s2} \quad \text{(S17)}$$

$$I_{s1bu} = [1 - l_i]\, \left[I_{s2tu} T_i + I_{s1bd}\, [1 - T_i]\right] \quad \text{(S18)}$$

$$I_{s1tu} = I_{s1bu} T_{s1} \quad \text{(S19)}$$

$$R_s = \left[1 - l_f\right]\, \left[I_0\left[1 - T_f\right] + I_{s1tu} T_f\right] \quad \text{(S20)}$$

Solving this system of equations allows to calculate the absorption

$$A_1 = ([1 - T_{d1}]\,[I_{d1td} + I_{d1bu}] + [1 - T_{s1}]\,[I_{s1td} + I_{s1bu}]) \,/\, (I_0 + G_1 + G_2) \qquad \text{(S21)}$$

in the top cell and in the absorption

$$A_2 = ([1 - T_{d2}][I_{d2td} + I_{d2bu}] + [1 - T_{s2}][I_{s2td} + I_{s2bu}])/\,(I_0 + \ G_1 + G_2) \qquad \text{(S22)}$$

in the bottom cell. The absorption in the back reflector is

$$A_b = [I_{d2bd} + I_{s2bd}]\,[1 - R_b] \,/\, [I_0 + G_1 + G_2] \ , \qquad \text{(S23)}$$

and the total reflection is

$$R = R_d + R_s. \qquad \text{(S24)}$$

Optics under solar light

For calculating the absorption under solar light, we choose $I_0 = 1$ and $G_1 = \ G_2 = 0$. Solving the equation system (S3) through (S20) gives analytic expressions for all the intensities encircled in Figure S1. This in turn yields analytic expressions for the absorptions and reflection given by (S21) through (S24) in terms of $\alpha_1, \alpha_2, T_{s1}, T_{s2}, T_{d1}, T_{d2}, n_0, n_1, n_2$, $T_f, T_i, R_b, l_f, l_i, l_b$. Please note that these parameters may depend on the wavelength. In what follows we only solve for the special case of zero Lambertian factor $l_i = 0$ at the interface between the top and the bottom cell. This leaves the parameters l_f and l_b to independently set the light trapping performance of the top and the bottom cell and also limits the complexity of the solution.

We provide the solutions of (S3) through (S20) in a plain text format for direct transfer from this supplementary to computer code by copy and paste. Please note: All variable names are identical to the naming in the main text when considering the following rules: (i) Subindices are written in line with the name of the variable, (ii) operations such as multiplication "*" and to the power "^" are explicitly written out, and (iii) the subindex "→" becomes a "To" also written in line as a part of the variable name. We use Mathematica 10 from Wolfram Research. Evaluating the absorption A_1 in the top cell from (S21) with the solution of the equation system we find

```
A1 = (Tf * ((-1 + lf) * (-1 + Ts1) * (1 + Ts1 - Ti * Ts1 - (-1 + lb) * Rb * (-1 + Ti -
Ts1 + 2 * Ti * Ts1) * Ts2^2) - (n1^2 * (-1 + Td1) * (-(lb * Rb * Td2 * (n1^2 * (1 +
Td1) - n0^2 * Td1 * Tf) * Ti^2 * Ts1 * Ts2) + lf * (n2^2 * (-1 + Rb * Td2^2) * (-1
+ Td1 * (-1 + Ti)) * (-1 + (-1 + lb) * Rb * (-1 + Ti) * Ts2^2) + Rb * Td2 * Ti * (-(lb
* n0^2 * Td1 * Tf * Ti * Ts1 * Ts2) + n1^2 * (1 + Td1) * (-Td2 + lb * Ti * Ts1 *
Ts2 + (-1 + lb) * Rb * Td2 * (-1 + Ti) * Ts2^2))))))/(-(n0^2 * n2^2 * Td1^2 * (-1 +
Rb * Td2^2) * Tf * (-1 + Ti)) + n1^4 * Rb * (-1 + Td1^2) * Td2^2 * Ti + n1^2 *
(n2^2 * (-1 + Rb * Td2^2) * (1 + Td1^2 * (-1 + Ti)) - n0^2 * Rb * Td1^2 * Td2^2
```

(S25)

* Tf * Ti))))/(1 + Rb * (-1 + lb + Ti - lb * Ti) * Ts2^2 + (-1 + lf) * (-1 + Tf) * Ts1^2 * (-1 + Ti + (-1 + lb) * Rb * (-1 + 2 * Ti) * Ts2^2))

for the absorption A_2 in the top cell.

The absorption in the bottom cell is derived from (S22) and reads

$$\begin{aligned}A2 = {} & (Tf * Ti *(-((-1 + lf) * Ts1 * (-1 + Ts2) * (-1 + (-1 + lb) * Rb * Ts2)) + ((-1 \\ & + Td2) * (lf * n1^2 * n2^2 * Td1 * (1 + Rb * Td2) - lb * (-1 + lf) * Rb * (-(n0^2 * \\ & n2^2 * Td1^2*(1 + Td2) * Tf * (-1 + Ti)) + n1^4 * (-1 + Td1^2) * Td2 * Ti + n1^2 \\ & * (n2^2 * (1 + Td2) * (1 + Td1^2 * (-1 + Ti)) - n0^2 * Td1^2 * Td2 * Tf * Ti)) * \\ & Ts1 * Ts2 - (-1 + lb) *lf *n1^2 * n2^2 * Rb * Td1 * (1 + Rb * Td2) * (-1 + Ti) * \\ & Ts2^2))/(-(n0^2 * n2^2 * Td1^2 * (-1 + Rb * Td2^2) * Tf *(-1 + Ti)) + n1^4 * Rb \\ & *(-1 + Td1^2) * Td2^2 * Ti + n1^2 * (n2^2 * (-1 + Rb * Td2^2) * (1 + Td1^2 * (- \\ & 1 + Ti)) - n0^2 * Rb * Td1^2 * Td2^2 * Tf * Ti))))/(1 + Rb * (-1 + lb + Ti – lb * \\ & Ti) * Ts2^2 + (-1 + lf) * (-1 + Tf) * Ts1^2 * (-1 + Ti + (-1 + lb) * Rb * (-1 + 2 * \\ & Ti) * Ts2^2)) \ .\end{aligned} \tag{S26}$$

From (S23) we find the parasitic absorption A_b in the back reflector to be

$$\begin{aligned}Ab = {} & -(((-1 + Rb) * Tf * Ti * (-((-1 + lf) * Ts1 * Ts2) + (Td2 * (lf * n1^2 * n2^2 * \\ & Td1 - lb * (-1 + lf) * Rb * Td2 * (-(n0^2 * n2^2 * Td1^2 * Tf * (-1 + Ti)) + n1^4 * \\ & (-1 + Td1^2) * Ti + n1^2 * (n2^2 * (1 + Td1^2 * (-1 + Ti)) - n0^2 * Td1^2 * Tf * \\ & Ti)) * Ts1 * Ts2 - (-1 + lb) * lf * n1^2 * n2^2 * Rb * Td1 * (-1 + Ti) * Ts2^2))/(n0^2 \\ & * n2^2 * Td1^2 * (-1 + Rb * Td2^2) * Tf * (-1 + Ti) - n1^4 * Rb * (-1 + Td1^2) * \\ & Td2^2 * Ti + n1^2 * (-(n2^2 * (-1 + Rb * Td2^2) * (1 + Td1^2 * (-1 + Ti))) + \\ & n0^2 * Rb * Td1^2 * Td2^2 * Tf * Ti))))/(1 + Rb * (-1 + lb + Ti - lb * Ti) * Ts2^2 \\ & + (-1 + lf) * (-1 + Tf) * Ts1^2 * (-1 + Ti + (-1 + lb) * Rb * (-1 + 2 * Ti) * Ts2^2))).\end{aligned} \tag{S27}$$

The total reflection $R_s + R_d$ follows from (S24) and is

$$\begin{aligned}Rs + Rd = {} & (1 - Tf - Ts1^2 + 2 * Tf * Ts1^2 + Ti * Ts1^2 - 2 * Tf * Ti * Ts1^2 + (lb \\ & * n0^2 * n1^2 * Rb * Td1 * Td2 * Tf^2 * Ti^2 * Ts1 * Ts2)/(n0^2 * n2^2 * Td1^2 \\ & * (-1 + Rb * Td2^2) * Tf * (-1 + Ti) - n1^4 * Rb * (-1 + Td1^2) * Td2^2 * Ti + n1^2 \\ & * (-(n2^2 * (-1 + Rb * Td2^2) * (1 + Td1^2 * (-1 + Ti))) + n0^2 * Rb * Td1^2 * \\ & Td2^2 * Tf * Ti)) - (-1 + lb) * Rb * (-1 + Tf + Ti - Tf * Ti + (-1 + 2 * Tf) * (-1 + 2 * \\ & Ti) * Ts1^2) * Ts2^2 + (lf * (n1^2 * (-1 + 2 * Tf) * (n2^2 * (-1 + Rb * Td2^2) * (1 \\ & + Td1^2 * (-1 + Ti)) + n1^2 * Rb * (-1 + Td1^2) * Td2^2 * Ti) * Ts1^2 * (-1 + Ti \\ & + (-1 + lb) * Rb * (-1 + 2 * Ti) * Ts2^2) + n0^2 * Td1 * Tf * (-(n2^2 * Td1 * (-1 + \\ & Rb * Td2^2) * (-1 + Ti) * (Tf + Ts1^2 - 2 * Tf * Ts1^2 - Ti * Ts1^2 + 2 * Tf * Ti * \\ & Ts1^2 + (-1 + lb) * Rb * (Tf - Tf * Ti + (-1 + 2 * Tf) * (-1 + 2 * Ti) * Ts1^2) * \\ & Ts2^2)) + n1^2 * Rb * Td2 * Ti * (Td1 * Td2 * (-Tf - (-1 + 2 * Tf) * (-1 + Ti) * \\ & Ts1^2) + lb * Tf * Ti * Ts1 * Ts2 - (-1 + lb) * Rb * Td1 * Td2 * (Tf - Tf * Ti + (-1 \\ & + 2 * Tf) * (-1 + 2 * Ti) * Ts1^2) * Ts2^2))))/(-(n0^2 * n2^2 * Td1^2 * (-1 + Rb * \\ & Td2^2) * Tf * (-1 + Ti)) + n1^4 * Rb * (-1 + Td1^2) * Td2^2 * Ti + n1^2 * (n2^2 *\end{aligned} \tag{S28}$$

(-1 + Rb * Td2^2) * (1 + Td1^2 * (-1 + Ti)) - n0^2 * Rb * Td1^2 * Td2^2 * Tf * Ti)))/(1 + Rb * (-1 + lb + Ti - lb * Ti) * Ts2^2 + (-1 + lf) * (-1 + Tf) * Ts1^2 * (-1 + Ti + (-1 + lb) * Rb * (-1 + 2 * Ti) * Ts2^2)) .

We successfully checked that the solution satisfies energy conversion $I_0 = A_1 + A_2 + A_b + R_s + R_d$.

Optics under luminescence from the top cell

The top cell of the tandem device can generate light that is absorbed in the bottom cell. Emission of luminescence light occurs at any location in the top cell in any direction. However, the optical model sketched in Figure S1 has no spatial resolution within the cells. It only knows the light intensities at the interfaces. We therefore calculate the thermal emission Flux G_1 at either interface. This flux originates from radiative recombination in the cell that is emitted in any direction and reaches either interface before interacting with the interfaces.

Photon flux from luminescence reaching the interfaces

Consider cell $i \in \{1,2\}$ in the dark at thermal equilibrium. There is a detailed balance of generation and recombination processes at any position and in any direction of light propagation: Photon absorption balances photon emission. No net photon flux leaves the cell through any element of the two surfaces fo cell i. The equilibrium photon flux density $(\mathrm{m}^{-2}\mathrm{s}^{-1})$ anywhere inside the cell is

$$\pi\, n_i^2\ \ \Phi_{bb} \tag{S29}$$

with

$$\Phi_{bb} = \frac{2c}{\lambda^4 \exp\left(\frac{h\,c}{\lambda\, q\, V_{th}}\right) - 1} \tag{S30}$$

denoting the vacuum black body photon flux per wavelength interval, per area and per solid angle in $(\mathrm{m}^{-2}\mathrm{s}^{-1})$. Now consider a planar surface inside cell i at one of the two surfaces. The equilibrium flux propagating into the cell i is also given by (S29). A fraction $\left(1 - T_{di}(W_i)\right)$ of this flux is absorbed during a single pass through the cell of thickness W_i. See (S2) in the supplementary material for details on the function T_{di}. Now assume that this inwards flux $\pi\, n_i^2\ \ \Phi_{bb}$ could be switched off. All photon absorption processes of the inward flux would then not exist and could no longer balance their emission counter-parts. The net emitted photon flux reaching the planar surface from these emission processes would therefore amount to

$$G_i = \pi\, n_i^2\ \ \Phi_{bb}\left(1 - T_{di}(W_i)\right). \tag{S31}$$

Any emission process from within the cell that reaches the surface element contributes to the emitted flux G_i because it's the inverse process did contribute to the absorbed flux. Using (S2) from the supplementary material we conclude that the flux emitted from within the cell to either surface of the cell is

$$G_i = \pi\, n_i^2 \;\; \Phi_{bb}\, E_{lum}(\alpha_i\, W_i) \tag{S32}$$

with

$$E_{lum}(x) := \; 1 - \; (1 - \mathrm{x})\, \exp(-\mathrm{x}) \;\; + \; \mathrm{x}^2\, E_1(\mathrm{x}). \tag{S33}$$

There are no interactions of this emitted flux with the interfaces.

Destinations of luminescence flux from the bottom cell

Next, we require an expression for the probability $A_{1\to 2}$ for absorption of this luminescence flux $2\, G_1$. The luminescent coupling current density will then be $(2\, G_1\, A_{1\to 2})$ with the factor 2 due to the two fluxes up- and downwards. While the upward flux is not directly absorbed in the bottom cell reflection at interfaces can redirect upwards luminescence to the bottom cell. We find $A_{1\to 2}$ when solving the above equations (S3) through (S20) for $G_1 = 1$ and $G_2 = I_0 = 0$. Renaming A_2 from (S22) to $A_{1\to 2}$ distinguishes the case of internal light generation in the top cell 1 from the case with external illumination. For the same reason A_b from (S23) is renamed to $A_{1\to b}$, and $R_s + R_d$ from (S24) to $A_{1\to 0}$. Text code for programming these quantities are given by (S34) through (S36) :

The loss of luminescence photons $A_{1\to 0}$ to the outside follows from (S24) and is

$$\begin{aligned}\mathrm{A1To0} = {} & (\mathrm{n0\hat{}2} * \mathrm{Tf} * (\mathrm{n2\hat{}2} * (-1 + \mathrm{Rb} * \mathrm{Td2\hat{}2}) * (-1 + \mathrm{Td1} * (-1 + \mathrm{Ti})) + \mathrm{n1\hat{}2} \\ & * \mathrm{Rb} * (1 + \mathrm{Td1}) * \mathrm{Td2\hat{}2} * \mathrm{Ti}))/(2 * (\mathrm{n0\hat{}2} * \mathrm{n2\hat{}2} * \mathrm{Td1\hat{}2} * (-1 + \mathrm{Rb} * \mathrm{Td2\hat{}2}) * \\ & \mathrm{Tf} * (-1 + \mathrm{Ti}) - \mathrm{n1\hat{}4} * \mathrm{Rb} * (-1 + \mathrm{Td1\hat{}2}) * \mathrm{Td2\hat{}2} * \mathrm{Ti} + \mathrm{n1\hat{}2} * (-(\mathrm{n2\hat{}2} * (-1 + \mathrm{Rb} \\ & * \mathrm{Td2\hat{}2}) * (1 + \mathrm{Td1\hat{}2} * (-1 + \mathrm{Ti}))) + \mathrm{n0\hat{}2} * \mathrm{Rb} * \mathrm{Td1\hat{}2} * \mathrm{Td2\hat{}2} * \mathrm{Tf} * \mathrm{Ti}))\,.\end{aligned} \tag{S34}$$

We find from (S22) for the absorption $A_{1\to 2}$ of luminescence from cell 1 in cell 2

$$\begin{aligned}\mathrm{A1To2} = {} & (\mathrm{n2\hat{}2} * (-1 + \mathrm{Td2}) * (1 + \mathrm{Rb} * \mathrm{Td2}) * (\mathrm{n1\hat{}2} * (1 + \mathrm{Td1}) - \mathrm{n0\hat{}2} * \mathrm{Td1} * \\ & \mathrm{Tf}) * \mathrm{Ti})/(-2 * \mathrm{n0\hat{}2} * \mathrm{n2\hat{}2} * \mathrm{Td1\hat{}2} * (-1 + \mathrm{Rb} * \mathrm{Td2\hat{}2}) * \mathrm{Tf} * (-1 + \mathrm{Ti}) + 2 * \mathrm{n1\hat{}4} \\ & * \mathrm{Rb} * (-1 + \mathrm{Td1\hat{}2}) * \mathrm{Td2\hat{}2} * \mathrm{Ti} + 2 * \mathrm{n1\hat{}2} * (\mathrm{n2\hat{}2} * (-1 + \mathrm{Rb} * \mathrm{Td2\hat{}2}) * (1 + \\ & \mathrm{Td1\hat{}2} * (-1 + \mathrm{Ti})) - \mathrm{n0\hat{}2} * \mathrm{Rb} * \mathrm{Td1\hat{}2} * \mathrm{Td2\hat{}2} * \mathrm{Tf} * \mathrm{Ti}))\,.\end{aligned} \tag{S35}$$

Absorption $A_{1\to b}$ of luminescence light from cell 1 may also occur in the back reflector. This absorption follows from (S23) and is

$$\begin{aligned}\mathrm{A1Tob} = {} & (\mathrm{n2\hat{}2} * (-1 + \mathrm{Rb}) * \mathrm{Td2} * (\mathrm{n1\hat{}2} * (1 + \mathrm{Td1}) - \mathrm{n0\hat{}2} * \mathrm{Td1} * \mathrm{Tf}) * \mathrm{Ti})/(- \\ & 2 * \mathrm{n0\hat{}2} * \mathrm{n2\hat{}2} * \mathrm{Td1\hat{}2} * (-1 + \mathrm{Rb} * \mathrm{Td2\hat{}2}) * \mathrm{Tf} * (-1 + \mathrm{Ti}) + 2 * \mathrm{n1\hat{}4} * \mathrm{Rb} * (-1\end{aligned} \tag{S36}$$

+ Td1^2) * Td2^2 * Ti + 2 * n1^2 * (n2^2 * (-1 + Rb * Td2^2) * (1 + Td1^2 * (-1 + Ti)) - n0^2 * Rb * Td1^2 * Td2^2 * Tf * Ti)) .

We successfully checked that the solution satisfies energy conversion $G_1 = A_{1\to0} + A_{1\to1} + A_{1\to2} + A_{1\to b}$.

Optics under luminescence from the bottom cell

The opposite case is luminescence generated in the bottom cell 2 that is absorbed in the top cell 1. Due to the smaller bandgap of cell 2 this contribution is typically negligible. For completeness we also solve the equation system (S3) through (S20) for this case with $G_2 = 1$ and $G_1 = I_0 = 0$. We rename A_1 from (S21) to $A_{2\to1}$, A_2 from (S22) to $A_{2\to2}$, A_b from (S23) to $A_{2\to b}$, and $R_s + R_d$ from (S24) to $A_{2\to0}$. The text codes for programming these quantities are given in (S37) through (S39).

The loss of luminescence photons $A_{1\to0}$ to the outside follows from (S24) and is

A2To0 = (n0^2 * n1^2 * Td1 * (1 + Rb * Td2) * Tf * Ti)/(2 * (n0^2 * n2^2 * Td1^2 * (-1 + Rb * Td2^2) * Tf * (-1 + Ti) - n1^4 * Rb * (-1 + Td1^2) * Td2^2 * Ti + n1^2 * (-(n2^2 * (-1 + Rb * Td2^2) * (1 + Td1^2 * (-1 + Ti))) + n0^2 * Rb * Td1^2 * Td2^2 * Tf * Ti))) . (S37)

We find from (S21) the absorption $A_{2\to1}$of luminescence light from cell to in cell a

A2To1 = ((-1 + Td1) * (1 + Rb * Td2) * (n1^4 * (1 + Td1) - n0^2 * n1^2 * Td1 * Tf) * Ti)/(-2 * n0^2 * n2^2 * Td1^2 * (-1 + Rb * Td2^2) * Tf * (-1 + Ti) + 2 * n1^4 * Rb * (-1 + Td1^2) * Td2^2 * Ti + 2 * n1^2 * (n2^2 * (-1 + Rb * Td2^2) * (1 + Td1^2 * (-1 + Ti)) - n0^2 * Rb * Td1^2 * Td2^2 * Tf * Ti)). (S38)

Absorption $A_{2\to b}$ of luminescence light from cell 2 may also occur in the back reflector. This absorption follows from (S23) and is

A2Tob = -((-1 + Rb) * (-(n0^2 * n2^2 * Td1^2 * (1 + Td2) * Tf * (-1 + Ti)) + n1^4 * (-1 + Td1^2) * Td2 * Ti + n1^2 * (n2^2 * (1 + Td2) * (1 + Td1^2 * (-1 + Ti)) - n0^2 * Td1^2 * Td2 * Tf * Ti)))/(2 * (n0^2 * n2^2 * Td1^2 * (-1 + Rb * Td2^2) * Tf * (-1 + Ti) - n1^4 * Rb * (-1 + Td1^2) * Td2^2 * Ti + n1^2 * (-(n2^2 * (-1 + Rb * Td2^2) * (1 + Td1^2 * (-1 + Ti))) + n0^2 * Rb * Td1^2 * Td2^2 * Tf * Ti))). (S39)

Again, we successfully checked that the solution satisfies energy conversion $G_2 = A_{2\to0} + A_{2\to1} + A_{2\to2} + A_{2\to b}$. The term $A_{2\to2}$ is the absorption of luminescence light from cell 2 in cell 2 for the second and subsequent passes and is not given here as it is only required for the energy conservation test.

Current voltage curves

Generation current density from solar absorption

The photogeneration current (in mA/cm^2) under external solar illumination is

$$J_{sc,i} = \frac{q}{h\,c} \int_{\lambda=0}^{\infty} \lambda\ A_i\ \Phi_{AM1.5G}\ d\lambda \tag{S40}$$

for $i \in \{1,2\}$ with $\Phi_{AM1.5G}$ being the solar AM1.5G spectrum (in W m^{-2} nm^{-1}).

Recombination current density of the top cell 1

We define the thermal current densities

$$J_{0,1\to x} = q\ \int_{\lambda=0}^{\infty} 2\ G_1\ \ A_{1\to x}\ \ d\lambda = q\ \int_{\lambda=0}^{\infty} 2\,\pi\,n_1^2\ \Phi_{bb}\ \ A_{1\to x}\ E_{lum}(\alpha_1 W_1)\ d\lambda \tag{S41}$$

of cell 1 with $x\epsilon\ \{0,\ 2, b\}$. The factor $\pi\,n_1^2$ is from the projected étendue of thermal recombination radiation in cell 1. Note that the factor $A_{1\to 0}$ from (S34) makes $J_{0,1\to 0}$ proportional to $n_0^2\ T_f$ as expected. With this, the recombination current density (in fA/cm^2)

$$\begin{aligned} J_{0,1} &= J_{0,1\to 0} + J_{0,1\to 2} + J_{0,1\to b} \\ &+ \left({Q_{i,1}}^{-1} - 1\right)\ \ q \int_{\lambda=0}^{\infty} W_1\ \alpha_1\ 4\,\pi\,n_1^2\ \Phi_{bb}\ d\lambda \end{aligned} \tag{S42}$$

of the top cell 1 is composed of the following contributions:

The three terms in the first line describe all radiative recombination. Following ref. [35], the photons flux from radiative recombination not being re-absorbed in cell 1 is equal to the sum of the flux that escapes to the outside $J_{0,1\to 0}/q$ plus the flux being parasitically absorbed either in the bottom cell ($J_{0,1\to 2}/q$) or in the back reflector ($J_{0,1\to b}/q$). The factor $A_{1\to 2}$ is proportional to T_i and makes $J_{0,1\to 2}$ vanish only for $T_i = 0$. The luminescent coupling term $J_{0,1\to 2}$ must therefore not be forgotten as it sometimes happened in the literature.[5,11,16]

The term containing $({Q_{i,1}}^{-1} - 1)$ in the second line of (S42) describes the non-radiative recombination in the top cell 1 as also described in ref. [35]. The material of the top cell is assumed to have an injection independent internal luminescence efficiency Q_{i1}. By definition Q_{i1} is the dimensionless ratio of radiative to total recombination rate. The factor $4\,\pi\,n_1^2$ stems from luminescence propagating into the full solid angle in cell 1.

Note that our definition of to $J_{0,1\to 0}$ by (S41) is different from the form $J_{0,1\to 0} = q\ \int_{\lambda=0}^{\infty} \pi\,n_0^2\ \Phi_{bb}\ A_1\ \ d\lambda$ as typically derived from the principle of detailed balance. However, both expressions are equivalent. We check this numerically for a few examples and find that the equality

$$2\,\pi\,n_1^2\,\Phi_{bb}\;\;A_{1\to 0}\,E_{lum}(\alpha_1 W_1) = \pi\,n_0^2\,\Phi_{bb}\,A_1 \tag{S43}$$

holds for all wavelengths if and only if the front surface of the top cell is Lambertian and thus $l_f = 1$.

Recombination current density of the bottom cell 2

With the definition of the thermal current densities

$$J_{0,2\to x} = q\;\int_{\lambda=0}^{\infty} 2\,\mathrm{G}_2\;\;A_{2\to x}\;\;d\lambda = q\;\int_{\lambda=0}^{\infty} 2\,\pi\,n_2^2\,\Phi_{bb}\,E_{lum}(\alpha_2 W_2)\;\;A_{2\to x}\;\;d\lambda\,. \tag{S44}$$

and $x\epsilon\,\{0,\;2, b\}$, the recombination current of the bottom cell (in fA/cm^2)

$$J_{0,2} = J_{0,2\to 0} + J_{0,2\to 1} + J_{0,2\to b} + J_{0SRH,2} \tag{S45}$$

also has four contributions. The first three correspond to those just discussed for cell1. The fourth contribution

$$J_{0SRH,2} = \frac{W_2}{150\ \mu\mathrm{m}}\,J_{0\mathrm{b},130} + J_{0\mathrm{s}} \tag{S46}$$

is non-radiative Shockley-Read-Hall recombination. The bulk recombination par is proportional to the thickness W_2. Here, $J_{0\mathrm{b},150}$ is the bulk recombination current of a 150 µm-thick Si wafer. The surface recombination current $J_{0\mathrm{s}}$ is independent of W_2 and accounts for recombination at both surfaces of the bottom cell. Auger recombination $J_{Aug}(V_2, W_2)$ has also has to be considered for Si. It increases linearly with the thickness W_2 and depends on quasi-Fermi level splitting V_2. We determine $J_{Aug}(V_2, W_2)$ numerically.[9]

Current-voltage curves and power conversion efficiencies

The current-voltage curve of the top cell 1

$$J_1 = J_{sc,1} + J_{0,2\to 1}\left(e^{\frac{V_2}{V_{th}}} - 1\right) - J_{0,1}\left(e^{\frac{V_1}{V_{th}}} - 1\right) \tag{S47}$$

shows a short circuit current density at $V_1 = 0$ that is increased by luminescent coupling current density $J_{2\to 1} = J_{0,2\to 1}\left(e^{\frac{V_2}{V_{th}}} - 1\right)$. Inspecting (S45) reveals that the corresponding

loss of carriers in cell 2 is the contribution of $J_{0,2\rightarrow1}$ to the $J_{0,2}\left(e^{\frac{V_2}{V_{th}}}-1\right)$. Carrier respectively photon conservation is thus given. Similarly, the current-voltage curve of a bottom Si cell is

$$J_2 = J_{sc,2} + J_{0,1\rightarrow2}\left(e^{\frac{V_1}{V_{th}}}-1\right) - J_{0,2}\left(e^{\frac{V_2}{V_{th}}}-1\right) - J_{Aug}(V_2,W_2)\,. \tag{S48}$$

The power conversion efficiencies

$$\eta_i(V_1,V_2,W_1,W_2,\lambda_c\ ) = \frac{V_i\ J_i(V_1,V_2,W_1,W_2,\lambda_c\ )}{1000\ \mathrm{W/m^2}} \tag{S49}$$

of the two cells $i \in \{1,2\}$ are thus a function of the two internal voltages V_i, the two thickness values W_i, and the cut of wavelengths of the filter λ_c at the intermediate interface. We filter transmission

$$T_i(\lambda,\lambda_c) = 0.5\left(1+\tanh\left(\frac{\lambda-\lambda_c}{\Delta\lambda}\right)\right) \tag{S50}$$

only allows wavelengths $\lambda > \lambda_c$ to pass and is a perfect reflector for $\lambda < \lambda_c$. We use $\Delta\lambda = 1\ \mathrm{nm}$. For calculating the maximum efficiency

$$\eta_x(V_1,V_2,W_1,W_2,T_i\ ) = \eta_1(V_1,V_2,W_1,W_2,T_i\ ) + \eta_2(V_1,V_2,W_1,W_2,T_i\ ) \tag{S51}$$

of the tandem cell we optimize η_x as a function of the five variables V_1, V_2, W_1, W_2, and $T_i \epsilon [0,1]$. We distinguish $x = 4T$ and $x = 2T$ for four terminal (4T) tandem cells and for two terminal (2T) tandem cells, respectively. For the 2T case the constraint

$$J_1(V_1,V_2,W_1,W_2,T_i\ ) = J_2(V_1,V_2,W_1,W_2,T_i\ ) \tag{S52}$$

is active when optimizing $\eta_{2T}(V_1,V_2,W_1,W_2,T_i\ )$, while this constraint is inactive when optimizing $\eta_{4T}(V_1,V_2,W_1,W_2,T_i\ )$.

Following ref.[15] we define the luminescent coupling efficiency

$$\eta_{LC} = \frac{J_{0,1\rightarrow2}}{J_{0,1\rightarrow0}} \tag{S53}$$

as the ratio of the emission current density to the outside over the generation current density in the bottom cell. Note, that the fraction of luminescence photons entering the bottom then is $\eta_{LC}/(1+\eta_{LC})$.

There are two major contributions to the luminescence absorbed in the bottom cell. First, the luminescence emitted towards the bottom cell. This component is proportional to $\left(1-T_{d1}(W_1)\right)T_i$. Second, luminescence light that is originally emitted towards the sun

and reverses direction when being reflected at the top cells' front surface. This light is then attenuated by a factor $T_{d1}(W_1)$ before passing the interface to the bottom cell. This contribution is $\left(1-T_{d1}(W_1)\right)\left(1-\ T_f\ n_0^2/n_1^2\right)\ T_{d1}(W_1)\ T_i$. As the luminescence emitted through the front surface is $\left(1-T_{d1}(W_1)\right)\ \ n_0^2/n_1^2\ T_f$, we find

$$\eta_{LC} = n_1^2 + (n_1^2 - 1)\, T_{d1}(W_1) \tag{S54}$$

for luminescence coupling efficiency, when assuming $T_i = T_f = n_0 = 1$. The blue line in Figure 1 (f) shows this theoretical single-wavelength estimation when evaluated at $E_{g1} + q\ V_{th}/2$, which is approximately the maximum of the luminescence spectrum. It reproduces the trends of the accurate calculation well. Equation (S54) may thus serve as physics-motivated estimation of the luminescence efficiency if the effort of applying the full model is too large. The generalization of (S54) to non-unity T_i and T_f is obvious.

The external quantum efficiency is defined as

$$Q_e = \frac{J_{0,1\to 0}}{J_{0,1}}. \tag{S55}$$

Parameter selected for a perovskite-silicon tandem device

Silicon data

Optical data and recombination parameters of the bottom Si cell are well documented in the literature. Here we apply the set of data that was previously applied to determine the Lambertian efficiency limit with a detailed balance modelling.[9] The more recent parametrization of Si Auger recombination[10] led to an Si efficiency benchmark efficiency of 29.4%. This is exactly reproduced by our model when setting the thickness to zero. Referring to (S45) we neglect Shockley-Read-Hall recombination in the base and at the surfaces of the bottom cell ($J_{0\mathrm{b},130} = J_{0\mathrm{s}} = 0$).

Perovskite data

We generate synthetical dielectric functions from the Baileys' oscillator parameterization.[18] For energy gaps E_{g1} ranging from 1.4 to 1.9 eV we multiply the bandgap and all resonance energies of Baileys' parametrization for $MAPbI_3$ with a common factor. This approach was introduced by Manzoor et al.[39] and was since then often applied for modelling tandem solar cells.[16,17]

Figure S2 shows the real and the imaginary parts of the complex index of refraction $(n + i\ k)$ generated this way. Scaling the bandgap and the oscillator energies also modifies the real part of the refractive index n in a Kramers-Kronig conform manner. This is

important for getting the luminescent coupling right because the escape cone of luminescence light is proportional to $1/n^2$.

Figure S3 shows the corresponding Tauc plots. In this work we label all band gaps by the intersection of linear fits to the Tauc with the energy axis, rather than by the value of the oscillator parameter representing the band gap. This is done to be conform with the gap labeling by experimentalists.

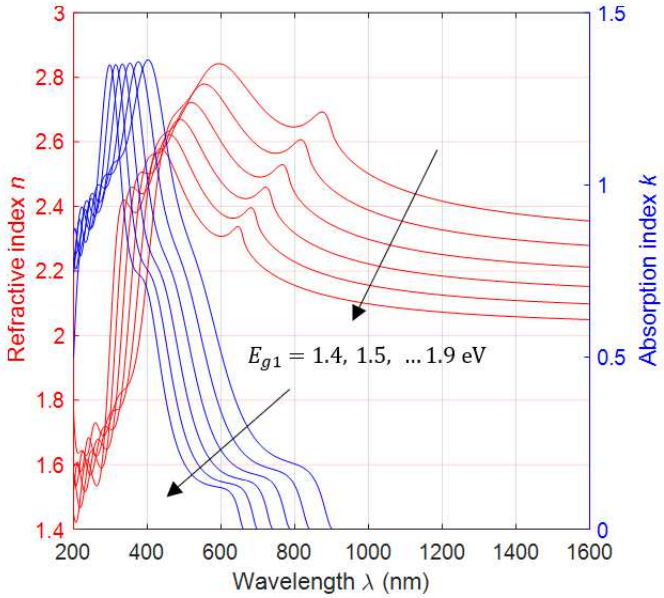

Figure S2: Modelled real part n *and imaginary part* k *of the complex index of refraction of the top cell with the band gap parameter* $\mathrm{E_{g1}}$ *varying from 1.4 (bottom) to 1.9 eV (top) in steps of 0.1 eV.*

In this paper we define the bandgap E_{g1} of the top cell as the energy value that results from a Tauc plot of $(\alpha\, E)^2$ versus photon energy E. While this approach has recently been critically reviewed[40] it is still laboratory practice in the field of perovskites. Figure S3 shows the Tauc plots generated from the modelled optical constants. We find an intersection with the energy axis that is consistently 27 meV larger that the bandgap parameter in the oscillator model. In what follows we therefore always report this intersection point as the bandgap energy E_{g1} for having a direct correspondence to the experimental praxis. The Forouhi-Bloomer model[41] was also used to model the dielectric function of $MAPbI_3$.[42] We decided for the Tauc-Lorentz model because the discrepancy in energy between the intersection of the Tauc plot and the bandgap parameter of the model is much larger than for the Tauc-Lorentz model.

Unless stated otherwise we make the following assumptions: The front surface transmission T_f is unity and so is the rear side reflectance R_b. We assume zero light scattering

$l_f = 0$ at the front surfaces: The top cell has no light trapping. The intermediate interface between the two cells is fully transparent with $T_i = 1$ at al wavelengths. Programmatically this is achieved by setting the filter cut off wavelength λ_c to $-1\ \mathrm{nm}$ in (S50). The internal luminescence efficiency is $Q_{i1} = 1$: The top cell only exhibits radiative recombination.

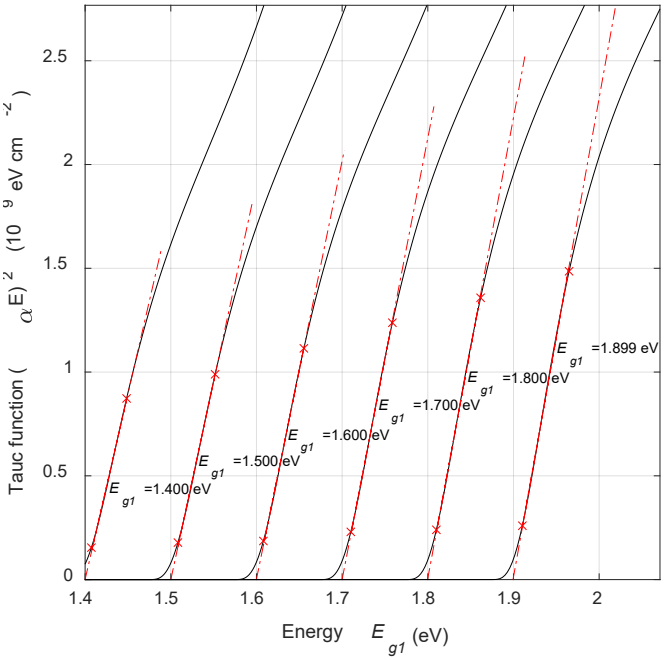

Figure S3: Energy gaps are labeled by the intersection points of the linear fit (dash dotted-read lines) to the Tauc plots (solid black lines). The intersection energies are 27 meV larger than the absorption onset. The latter equals the gap parameter of the Tauc-Lorentz model[19].